

# GPS displacement dataset for study of elastic surface mass variations

Athina Peidou<sup>1</sup>, Donald Argus<sup>1</sup>, Felix Landerer<sup>1</sup>, David Wiese<sup>1</sup> and Matthias Ellmer<sup>1</sup>  
Jet Propulsion Laboratory, California Institute of Technology, Pasadena, CA, USA, 2023

Correspondence to: Athina Peidou ([athina.peidou@jpl.nasa.gov](mailto:athina.peidou@jpl.nasa.gov))

© 2023. California Institute of Technology. Government sponsorship acknowledged.

## Abstract

Quantification of uncertainty in surface mass change signals derived from GPS measurements poses challenges, especially when dealing with large ~~datasets~~ with continental or global coverage. We present a new GPS station displacement ~~dataset~~ that reflect surface mass load signals and their uncertainties. We assess the structure and quantify the uncertainty of vertical land displacement derived from 3045 GPS stations distributed across the continental US. Monthly means of daily positions are available for 15 years. We list the required corrections to isolate surface mass signals in GPS estimates and screen the data using GRACE(-FO) as external validation. Evaluation of GPS timeseries is a critical step, which identifies a) corrections that were missed; b) sites that contain non-elastic signals (e.g., close to aquifers); and c) sites affected by background modelling errors (e.g., errors in the glacial isostatic model). Finally, we quantify uncertainty of GPS vertical displacement estimates through stochastic modeling and quantification of spatially correlated errors. Our aim is to assign weights to GPS estimates of vertical displacements, which will be used in a joint solution with GRACE(-FO). We prescribe white, colored and spatially correlated noise. To quantify spatially correlated noise, we build on the common mode imaging approach adding a geophysical constraint (i.e., surface hydrology) to derive an error estimate for the surface mass signal. We study the uncertainty of the GPS displacement ~~timeseries and find an average~~ noise level between 2-3 mm ~~when~~ white noise, flicker noise, and RMS of residuals about a seasonality and trend fit ~~are used to describe uncertainty~~. Prescribing random walk noise increases the error level such that half of the stations have noise > 4 mm, which is systematic with the noise level derived through modeling of spatial correlated noise. The new ~~dataset~~ is suitable for use in a future joint solution with GRACE(-FO)-like observations.

Keywords: GPS uncertainty | elastic displacement | GRACE-FO | surface mass change

## 1. Introduction

For more than two decades, the Gravity Recovery and Climate Experiment (GRACE) space gravity mission and its nearly identical successor mission, GRACE-Follow on (GRACE-FO), have provided mass change estimates through tracking the time-variable part of the Earth's gravity field (Landerer et al., 2020). Mass change products are typically given on a monthly basis and have been used to study a variety

Style Definition: Heading 1

Deleted: data set

Deleted: data set

Deleted: s

Deleted: , derived using each technique and find that three techniques exhibit

Deleted: :

Deleted: data set

47 of critical climate-related factors (Tapley et al., 2019), such as sea level rise (Frederikse et al., 2020); ice  
48 mass change (Velicogna et al., 2020); prolonged drought periods (Thomas et al., 2014) and regional flood  
49 potentials (Reager et al., 2014). The measurement geometry of GRACE(-FO) limits the study of  
50 geophysical processes to spatial scales of ~300 km and larger, for monthly timespans. Recent community  
51 reports (Pail et al., 2015, Wiese et al., 2022) have highlighted the utility and need of mass change  
52 observations at improved spatial resolutions to address a number of science and applications objectives.  
53 Examples include closure of the terrestrial water budget for small to medium sized river basins, and  
54 separation of surface mass balance from ice dynamic processes at the scale of individual outlet glacier  
55 systems.

56 The spatial resolution of gravity maps derived from satellite measurements is limited by sampling at  
57 altitude. Fusion with external geodetic data sources, however, can improve spatial resolution over what  
58 can be achieved only with satellite gravimetry. GPS position timeseries have been used widely to study  
59 the elastic response of Earth's surface to mass loading (e.g., Argus et al., 2017; Fu and Freymueller,  
60 2012) and can provide information at short wavelengths (~100km) (Argus et al., 2021). Solid Earth  
61 responds elastically to changes in the surface load of water, snow, ice, and atmosphere. When the Earth's  
62 surface is loaded with mass (e.g., snow and water) it subsides; and when mass loads are removed the  
63 surface rises. Thus, the Earth's response follows the water cycles such that: precipitation and snow  
64 accumulation cause subsidence of the surface and snow melt, evaporation and water run off allow the  
65 Earth's surface to bounce back (uplift). Focus is typically placed on the radial direction (vertical), due to  
66 the rapid decrease of vertical displacement with the distance from a surface load (Argus et al., 2017),  
67 which leads to high fidelity estimates in the space domain. Note that across certain geological formations  
68 such as aquifers, subduction zones and regions with volcanic activity surface loading is mixed with other  
69 solid Earth/geophysical processes making it difficult to isolate the elastic component. Therefore, GPS  
70 sites located at the vicinity of such formations are omitted.

71 GPS displacements between two epochs have many different signals embedded in them; i.e., those related  
72 to non-tidal atmospheric and oceanic loading, solid Earth phenomena such as tectonics, glacial isostatic  
73 adjustment, and others related to surface mass changes. With the proper treatment (see Sec.2) GPS  
74 stations can capture local surface mass changes. We are interested in isolating the signals that reflect the  
75 Earth's elastic response to mass variations, thus we apply a set of corrections to GPS vertical  
76 displacement estimates, and then we screen the data for outliers or potential errors. The data screening  
77 process checks for consistency between GPS and GRACE(-FO) vertical displacement estimates (similar  
78 analysis has been performed by Yin et al., 2020; Blewitt et al., 2001; van Dam et al., 2001; Becker and  
79 Bevis, 2004; Davis, 2004; Tregoning et al., 2009; Tsai, 2011 and Chew et al., 2014) and identifies outliers  
80 that statistical tests fail to pick up (He et al., 2018).

81 The last step is to estimate uncertainty in the screened dataset. Since our purpose is to isolate surface mass  
82 load signals, we define *error* as any vertical displacement signal that does not reflect an elastic surface  
83 mass load. The reported uncertainty reflects the sum of all error sources to the measurement and is the  
84 final product of this study. Error correlation (temporal and spatial) and the deficiency of stochastic noise  
85 models to describe the error realistically are the main challenges in this uncertainty quantification task.  
86 Error sources include errors driven by satellite antenna phase centre offsets (Haines et al., 2004;  
87 Santamaria-Gomez et al., 2012); atmospheric pressure models (Kumar et al., 2020); non-tidal ocean  
88 loading (Jiang et al., 2013); satellite orbits (Ray et al., 2008; Amiri-Simkooei, 2013); earth orientation  
89 parameters (Rodriguez-Solano et al., 2014); and tectonic trends and post-seismic relaxation after  
90 earthquake activity (Ji and Herring, 2013; Crowell et al., 2016).

Deleted: data set

Deleted: of a measurement

93 The GPS position-time series have common mode displacements [Tian and Shen 2016], including both a  
94 common mode error strongly varying each day and a common mode signal associated with seasonal water  
95 fluctuations. Wdowinski et al. (1997) first defined common mode error to be a series of rigid-body  
96 translations that reflect an error in the position of all geodetic sites in an area relative to an absolute  
97 reference frame; by removing the mean position (or stack) of all sites in an area, scientists recover more  
98 accurate estimates of relative position contained in the data. Dong et al. (2006) and Serpelloni et al.  
99 (2013) defined common mode error in a more sophisticated manner using principal or independent  
100 component analysis such that they remove spatially correlated, temporally incoherent error. Independent  
101 is different than principal component analysis in that it finds the maximum independence of the  
102 components instead of minimum correlation (Milliner et al., 2019; Liu et al., 2015). Common mode  
103 displacements includes both error (such as that associated with error in satellite orbits) and signal (such as  
104 the seasonal oscillation of elastic vertical displacement in elastic response to seasonal fluctuations in mass  
105 between the hemispheres) (Sun et al. 2016).  
106 Considering the increased number of GPS stations and the limitations posed by the existing  
107 methodologies, Kreemer and Blewitt (2021) used a robust methodology to estimate the common spatial  
108 components of GPS residuals (i.e., the remaining signals of a timeseries after subtraction of a trajectory  
109 model). A trajectory model is a model consisting of an offset, a rate, and a sinusoid with a period of 1  
110 year (Bevis and Brown, 2014). The so-called common mode component (CMC) imaging technique was  
111 originally introduced by Tian and Shen (2016) and quantifies the spatial correlation of the residuals  
112 (position or vertical displacement timeseries anomaly with respect to a trajectory model) of unequal-  
113 length timeseries using information from neighbor stations. It is important to note that CMC reflects both  
114 spatially correlated noise and spatially correlated signals, including elastic displacements, that a trajectory  
115 model fails to describe.  
116 Spectral analysis of the residuals (with respect to a trajectory model, see Eq.2) is an alternative way to  
117 estimate the noise level of vertical displacement series for each GPS station. The spectrum of the  
118 residuals can be approximated by white or colored noise (flicker, random walk, power law approximation,  
119 generalized gauss markov etc.), or by a combination of white and colored noise (Williams et al., 2004;  
120 Bos et al., 2008; Klos et al., 2014). A summary of the different noise models and their power distribution  
121 can be found in He et al. (2018). Several standard GPS timeseries analysis packages are available to  
122 perform such an analysis, e.g., the Create and Analyze Timeseries (CATS) (Williams, 2008) and Hector  
123 (Bos et al. 2013). Various studies in the past suggested that the residuals are better described by a  
124 combination of white and flicker noise (see e.g., Klos et al., 2014; Argus et al., 2017), with the latter  
125 contributing the most (Argus and Peltier, 2010). Recently, Argus et al. (2022), showed that the longer the  
126 timeseries the more the spectrum of GPS residuals converges with the noise model of random walk.  
127  
128 Here, we outline a comprehensive framework for processing large datasets (continental and/or global) of  
129 GPS timeseries, to derive estimates that only reflect surface mass signals, for use in a joint inversion with  
130 GRACE(-FO) measurements. Originally, we layout the corrections required to capture local surface mass  
131 changes (Section 2.1). Our interest is to make the process as automated as possible, thus we set a number  
132 of evaluation metrics to detect outliers among all candidate (for the joint inversion) sites. Stations flagged  
133 as outliers are further evaluated for extra corrections (e.g., offsets; poor site maintenance etc.). Finally, we  
134 assign weights to each GPS vertical displacement record. We test the most popular methodologies to  
135 quantify the error, considering time-correlation, spatial-correlation and/or white noise (Section 3). Note  
136 that for spatially correlated noise the commonly used PCA/ICA is not as applicable to our use case,

Deleted: Many of the error sources are “common mode” (also called common model noise, Tian and Shen 2016).

Deleted: l

Deleted: Common mode error may include both error

Deleted: time-series

Deleted: ¶

Deleted: time-series

Deleted: time-series

Deleted: time series

Deleted: Time Series

Deleted: data set

148 because our dataset extends over very large spatial areas (continental). CMC imaging (Kreemer and  
149 Blewitt; 2021) fits our needs better. We build on the existing CMC algorithm to remove hydrology  
150 signals from the error estimate by deriving surface loading signals from a hydrology model and removing  
151 them from the GPS vertical displacements (see Section 3 for more details). The final product is a new  
152 dataset with GPS vertical displacement estimates that reflect elastic mass variations and their  
153 uncertainties.

Deleted: data set

Deleted: up displacement

Deleted: data set

## 155 2. GPS data processing and screening

### 157 2.1 Isolating surface mass loading fingerprint from GPS vertical displacements

158 We analyze positions of 3054 GPS sites as a function of time from 2006 to 2021 estimated by scientists at  
159 the Nevada Geodetic Laboratory (NGL) (Blewitt et al. 2018). Technologists at Jet Propulsion Laboratory  
160 (JPL) first estimate satellite orbits, satellite clocks, and positions for a core set of roughly 50 sites on  
161 Earth's surface (Bertiger et al. 2020). NGL uses JPL's clock and orbit products and performs point  
162 positioning to a total of about 18,500 GPS sites distributed across the world. Following the International  
163 Earth Rotation Standards (IERS) (Petit and Luzum, 2012) NGL's positions are corrected for solid Earth,  
164 ocean, and pole tides. NGL's positions in International Terrestrial Reference Frame 2014 (ITRF2014)  
165 (Altamimi et al. 2016) are more accurate than NGL's previous estimates of positions in ITRF2008. NGL  
166 estimates GPS wet tropospheric delays each day using the ECMWF weather model (Simmons et al. 2007)  
167 and the VMF1 tropospheric mapping function (Boehm et al. 2006). We input the NGL position  
168 timeseries, derive the displacement relative to a reference epoch and then follow, Argus et al. (2010, 2017,  
169 2021) to isolate the part of GPS displacements reflecting solid Earth's elastic response.

Deleted:

Deleted: analyze GPS position-time series

Deleted: ing

Deleted: . To

Deleted: , we

Deleted: time series

171 a. Construct timeseries of elastic displacement uninterrupted by offsets due to antenna substitutions or  
172 earthquakes that pass through a specific reference time (such as Jan 1, 2014) by eliminating data before  
173 and /or after an offset.

175 b. Identify and omit GPS sites recording primarily i. poreoleastic response to change in groundwater, ii.  
176 strong volcanic fluctuations, and iii. postseismic transients following Argus et al. (2014, 2017, 2022). In  
177 the west U.S., GPS sites responding to groundwater change have maximum height around April when  
178 water is maximum, subside in the long term faster than 1.8 mm/yr, exhibit strong transients, and/or are  
179 located in known aquifers (Argus et al. 2014). Volcanic activity is readily identified by Interferometric  
180 Synthetic Aperture Radar (InSAR) and GPS observations of strong transients and anomalous sustained  
181 uplift or subsidence (Argus et al. 2014, Hammond et al. 2016).

183 c. Remove non-tidal atmospheric (NTAL) and non-tidal oceanic (NTOL) mass loading by interpolating  
184 global grids of elastic displacements calculated by the German Center for Geoscience (GFZ) (Dill  
185 Dobslaw, 2013) following the method of Martens et al. (2020).

187 d. Remove glacial isostatic adjustment as predicted by model ICE-6G\_D (VM5a) (Peltier et al. 2015,  
188 2018; Argus et al. 2014).

190 e. Remove interseismic strain accumulation associated with locking of the Cascadia subduction zone  
191 using an upgrade of the model of Wang et al. (2018). The model is superposition of 2/3 of the elastic and

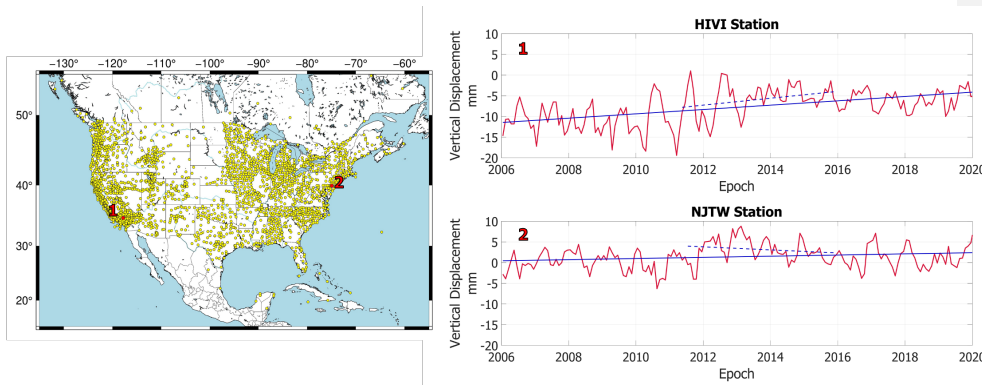
201 1/3 of the viscoelastic model of Wang et al. (2018). We communicated with Li Wang and his team at  
 202 National Resources Canada, that the Wang et al. (2018) model does not fit the available GPS data; they  
 203 have produced an interim model using our input that more nearly fits the GPS data.

204  
 205 f. Average the daily estimates of GPS vertical displacements into monthly means centered at the center of  
 206 each month from January 2006 to June 2021.

207  
 208 To compare GPS with GRACE(-FO) vertical displacement estimates we reference the series to the epoch  
 209 with the most GPS site records, which is September 2012. This process results in an 11% loss of stations  
 210 (i.e., no available measurement on 09/2012). Similar to Yin et al. (2020), detrended monthly estimates of  
 211 each station that are larger than  $3\sigma$  relative to the mean of the timeseries are considered outliers and  
 212 removed from the dataset. Statistical outliers comprise  $\sim 0.5\%$  of the records.

213 2705 (or 88.8%) of GPS stations remain after the choice of reference epoch, the  $3\sigma$  test and the removal  
 214 of sites with non-elastic loading response. The distribution of sites is denser along the East and West  
 215 coasts, and fairly sparse in the central-north US (Fig. 1). Series of two arbitrary stations (HIVI and NJWT)  
 216 located at the West and East coast respectively, are shown in Fig. 1. The response of the Earth on the  
 217 extensive drought period in California between 2011.5-2015.5 is captured in the uplift trend mapped by  
 218 HIVI station (Fig. 1, top right panel; dashed blue line).

219



220  
 221 Figure 1: Left panel) Map of study area. GPS stations are shown in yellow; Right panel) Vertical  
 222 displacement timeseries of two random stations (red line). Solid blue line denotes the overall trend of the  
 223 timeseries and dashed blue line the trend between (2011.5-2015.5). Note the significant uplift of the HIVI  
 224 station located in southern California.

225  
 226 2.2 External validation datasets - Time-variable gravity field

227  
 228 We compare GPS observations of vertical displacement against GRACE(-FO) estimates of solid Earth's  
 229 elastic vertical displacement from terrestrial water, snow, and ice.

230 To compare to GRACE(-FO), we analyze JPL's three-degree mascon solution (Release 6, Watkins et al.  
 231 2015, Wiese et al. 2016). The effect of glacial isostatic adjustment is removed from GRACE(-FO)  
 232 products using ICE-6G\_D model estimates (Peltier et al., 2017). The geocentre motion (degree 1)

Deleted: position

Deleted: time-series

Deleted: data set

Deleted: hivi

Deleted: njwt

Deleted: hivi

Deleted: hivi

Deleted: data set

241 coefficient is using the technique of Sun et al. (2016) (Technical Note 13). Values of C20 (Earth's  
 242 oblateness) and C30 (for months after Aug 2016) are substituted with SLR data (Loomis et al., 2019). We  
 243 calculate solid Earth's elastic response by using the loading Love number of the Preliminary Reference  
 244 Earth Model (Wang et al.; 2012).  
 245 Estimates of GPS positions in ITRF2014 (Altamimi et al. 2016) are relative to center of mass (CM) in the  
 246 long term but relative to center of figure (CF) in the seasons (because ITRF2014 does not allow there to  
 247 be seasonal oscillations of CM). We therefore remove the long-term rate of CM relative to CF to  
 248 transform the GRACE estimates in the long term from CF to CM (but do not remove seasonal oscillations  
 249 of CM relative to CF so as to preserve the ITRF seasonal frame relative to CF). The annual signal of the  
 250 geocenter (as realized by ITRF 2014) projected on the up component in north America on average  
 251 explains 3% of the GPS vertical displacement signal and can explain up to 20% for certain sites.  
 252 GRACE(-FO) vertical displacement monthly estimates are derived as follows (e.g., Davis et al., 2004):  
 253

$$U(\phi, \lambda) = a \sum_{lm} \left( \frac{h_l^E}{1 + k_l^E} \right) P_{lm}(\sin\lambda) \times [C_{lm} \cos m\phi + S_{lm} \sin m\phi] \quad (1)$$

254 Where,  $U$  is the estimate of vertical displacement,  $a$  denotes the Earth's radius,  $\phi, \lambda$  denote the latitude  
 255 and longitude, respectively;  $P_{lm}$  are the associated Legendre polynomials,  $k_l^E$  and  $h_l^E$  are the elastic  
 256 gravity and vertical load Love numbers (Wang et al., 2012), respectively, and  $C$  and  $S$  are the spherical  
 257 harmonic coefficients derived from GRACE(-FO) monthly solutions with respect to degree  $l$  and order  
 258  $m$ . JPL releases gridded mascon fields, to derive spherical harmonics ( $C$  and  $S$  in Eq. 1). We transform  
 259 fields of equivalent water height to normalized harmonic coefficients using the inverse of Eq. 9 in Wahr  
 260 et al. (1998). Like GPS, we subtract the GRACE(-FO) vertical displacement field of September 2012  
 261 from each monthly field to establish a common reference basis. GRACE(-FO) fields are estimated at a  
 262 0.5-degree spatial resolution ( $\phi, \lambda$  in Eq.1). Thus, we extract GRACE(-FO) estimates at the station level  
 263 by interpolating bilinearly the vertical displacement from the nearest 0.5-degree grid point neighbors to  
 264 the station's location.  
 265

### 266 2.3 Screening metrics

267 GPS vertical displacement estimates are evaluated against the ones derived from GRACE(-FO), to assist  
 268 in identifying outliers or further corrections that may be needed. We employ a number of different metrics  
 269 to evaluate the agreement between the two datasets, and to determine whether to include it in the joint  
 270 solution or not. Similar to Yin et al. (2020) we quantify correlation and variance reduction between GPS  
 271 and GRACE(-FO) vertical displacements. The structure of surface mass periodic signals (e.g., annual  
 272 cycles, trends) as picked up by the two measurement techniques, also entails critical information  
 273 regarding mismodelled offsets, and is evaluated as well.  
 274

275 This process flags sites that need correction and corroborates joint inversion's hypothesis (Argus et al.,  
 276 2021), that a basic level of agreement is needed for the GPS data to be used to infer surface mass change.  
 277

### 278 *Correlation*

279  
280

Deleted:

Deleted: data set

283 First, we specify the level of agreement between the datasets by estimating the Pearson correlation  
284 coefficient between GPS and GRACE(-FO) timeseries. On average, correlation is 62%, but stations  
285 located on the West coast exhibit an agreement higher than 80%, which in most cases is driven by the  
286 larger annual signal amplitude there. A more detailed look into the correlation metric is performed to  
287 evaluate the agreement of GPS/GRACE(-FO) in retrieving the seasonal cycle amplitude in different  
288 watersheds. We fit and remove a trajectory model  $y(t)$ :

$$y(t) = a + bt + A\sin(2\pi t) + B\cos(2\pi t), \quad (2)$$

290  
291 with  $a$  being the intercept;  $b$  being the trend and  $A$  and  $B$  being the amplitudes of the sine and cosine  
292 components of a periodic function. In a future release of the dataset, we will evaluate the presence of  
293 draconitic periods in the time-series and add them in the trajectory model if justified. With the timespan  
294 of the current timeseries being up to 15 years, we cannot resolve for the draconitics (i.e., the first  
295 draconitic period (351.6 days) and the annual cycle (365.25 days) are very close and require a long time-  
296 series to be deciphered). For a more thorough discussion we refer the interested reader to Amiri-Simkooei  
297 et al. (2017) and Klos et al. (2023).

298  
299 We classify stations in watersheds and plot the GPS-GRACE(-FO) correlation coefficient ( $R$ ) of each  
300 station in different watershed against the amplitude of annual signals (Fig. 2b). To quantify the  
301 relationship between magnitude of the annual cycle and correlation between the two datasets we fit a  
302 linear function between the magnitude of the annual signals and the GPS-GRACE(-FO) vertical  
303 displacement correlations for each watershed, separately. A steep slope ( $\alpha$ ) of the fit ( $\alpha > 0.5$ ) indicates an  
304 agreement between the two datasets, which depends on the magnitude of the annual cycle. This  
305 relationship breaks when stations of a basin exhibit smaller annual cycles. We discuss an interesting case  
306 in Supplements, where stations located in the Great Lakes region (part of the St. Lawrence watershed)  
307 demonstrate a negative trend  $\alpha = -1.26$ . The disagreement is even more pronounced while assessing the  
308 second metric (i.e., trends). Both metrics, when taken together, helped us identify the source problem (i.e.,  
309 unlogged offset that affected nearly 25% of the stations located in the St. Lawrence watershed) and take  
310 corrective actions (see Supplements for more details). Note that for Figs. 2 and 3 the corrected data were  
311 used.

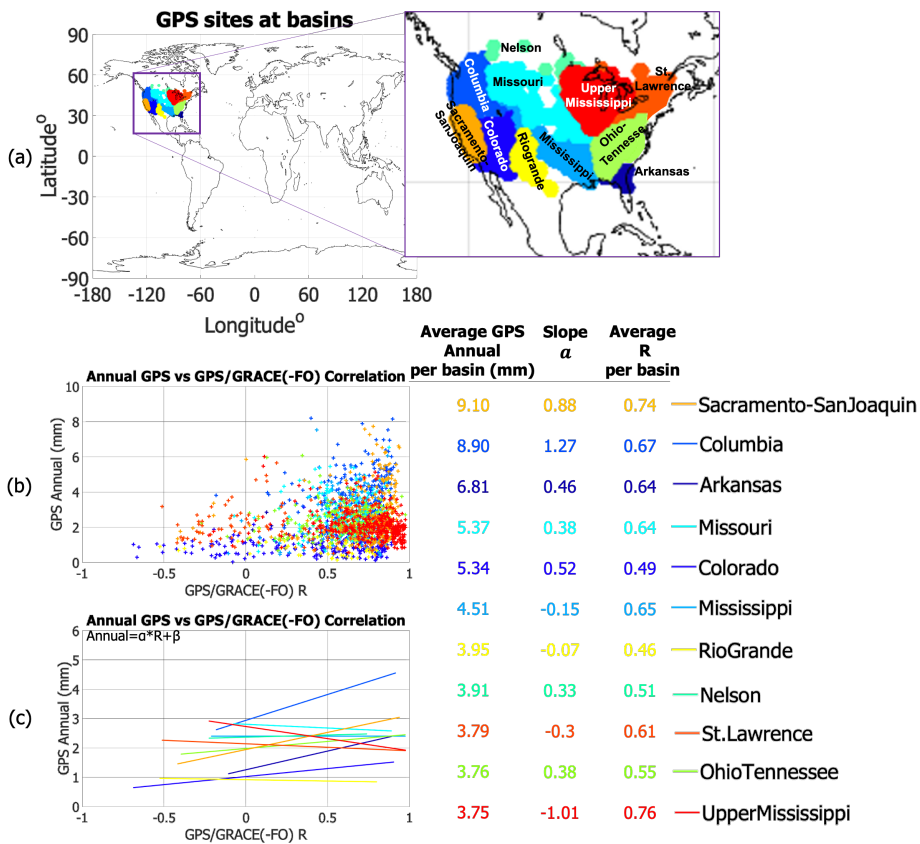
312  
313

Deleted: data set

Deleted: the

Deleted: data set

Deleted: data set



318  
 319  
 320 Figure 2: a) GPS sites clusters at watersheds in the US. Each watershed has a different color; b)  
 321 Magnitude of annual GPS vertical displacement cycles derived with respect to GPS-GRACE(-FO)  
 322 correlation; c) Linear fit between magnitude of the annual GPS vertical displacement cycles and GPS-  
 323 GRACE(-FO) correlation.

324  
 325 *Trends*

326  
 327 In order to study the agreement between GPS/GRACE(-FO) in more detail, we split the timeseries of each  
 328 station into non-overlapping intervals of 36 months, and fit Eq.2 for each station during each time-  
 329 window. Different time-lengths of the GPS series may lead to misinterpretation of the geophysical  
 330 content. For example, a station that has records only for the first 13 months out of the total of 36 months  
 331 window may reflect different fit constituents compared to a neighbor station with full records, if the  
 332 actual behavior of Earth's response changes during the 36-months window. Although in our [dataset](#) this

Deleted: data set



334 case is rare, we proceed with deriving the rate (slope) and the annual cycles only for stations that have  
335 records for at least 28 out of the 36 months. We did not interpolate the series during the GRACE(-FO)  
336 gap; thus, the last time-window reflects trends estimated using only GRACE(-FO) and GPS timeseries  
337 between June 2018-2021. As expected, GPS rates feature higher spatial variability than GRACE(-FO).  
338 However, both techniques capture large-scale quasi-periodic variations every 3 years (Fig. 3), an  
339 agreement that is noteworthy. The effect of this metric to detect outliers is pronounced when the two  
340 techniques show flipped trends.

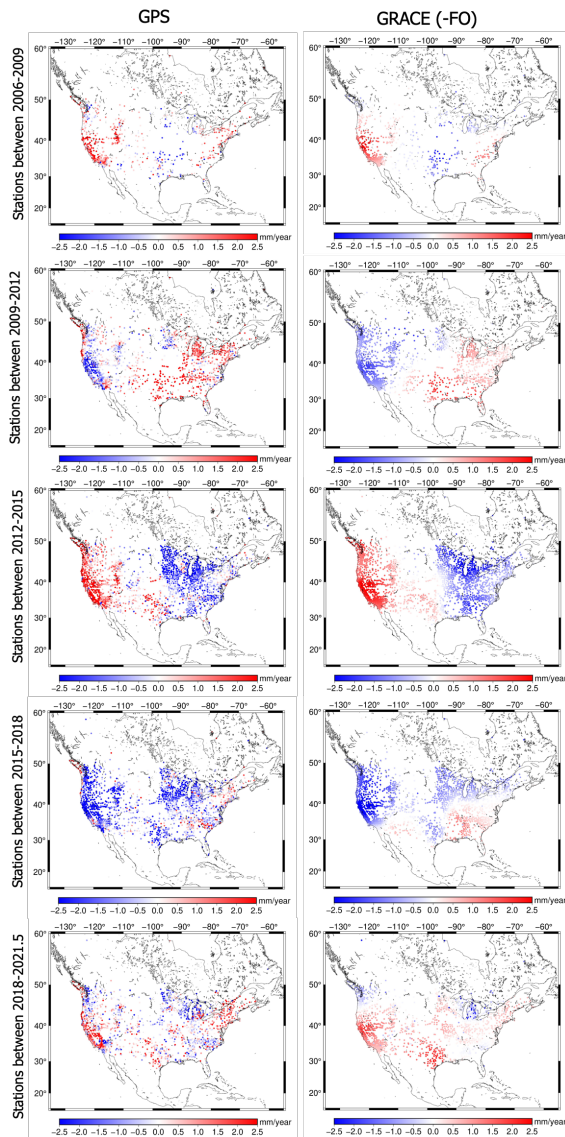
341

342 Regions with pronounced trend disagreement:

- 343 • St. Lawrence watershed (stations located in the Great Lakes region at the State of Michigan): The  
344 trend during 2015-2018 was flipped between GPS and GRACE(-FO) in 62 stations (St. Lawrence  
345 watershed has a total of 243 stations available between 2015-2018). We discovered a missed  
346 offset in the series occurring in April 2016, and corrected for it, which led to an improved  
347 agreement in the trend (see Supplements).
- 348 • Cascadia region (northwest coast): The disagreement is evident in maps spanning 2009-2012,  
349 2015-2018 and 2018-2021.5. GPS sites record a large surface uplift, which over the course of 15  
350 years sums to 60 mm in sites located in Vancouver Island. GRACE(-FO) does not capture any  
351 such behavior. We attribute this disagreement partly on 1) glacial isostatic adjustment modeling  
352 error which manifests oppositely on two techniques. ICE6G\_D predicts too much subsidence,  
353 thus when we correct GPS, we find too much uplift and when we correct GRACE(-FO) we find  
354 too much water gain which predicts too much subsidence; and partly on 2) the interseismic strain  
355 accumulation correction applied in the GPS ~~dataset~~ over this area (Argus et al., 2021). The sites  
356 have been flagged and are not going to be used in the joint inversion.
- 357 • San Andreas Fault (Southern California): Sites located in a vicinity of the Parkfield segment of  
358 the fault (Carrizon plain), exhibit consistent disagreement in the trend. More investigation is  
359 required to understand the mechanism that the fault presents on GPS/GRACE(-FO) vertical  
360 displacement estimates. The disagreement is also seen in Argus et al. (2022, Fig. S12). The sites  
361 have been flagged and are not going to be used in the joint inversion.

362

Deleted: data set



364  
 365 Figure 3: Rates of vertical displacements derived by GPS and GRACE. The rates are calculated every 36-  
 366 months (3 years) between 2006-2021.

367  
 368

369 *Variance Reduction*

370

371 Similarity in both amplitude and phase between two quantities is quantified via the variance attenuation  
372 factor (Gaspar and Wunsch, 1989; Fukumori et al., 2015):

373

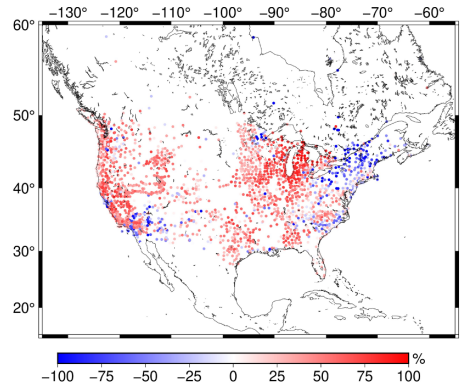
$$var_{red} = \left( 1 - \frac{var(GPS - GRACE(-FO))}{var(GPS)} \right) \times 100 \quad (3)$$

374

375 The higher the agreement in phase and amplitude between GPS and GRACE(-FO), the closer the metric  
376 gets to 100%.  $var_{red}$  may also be negative when the differences in amplitude and/or phase are large.

377 Overall, GPS and GRACE(-FO) are consistent when  $var_{red}$  exceeds 50%. The areas of main  
378 disagreement are near coasts, especially along the Atlantic Ocean. This inconsistency can be partly  
379 explained by modeling errors of the non-tidal oceanic and atmospheric loading model (e.g., Klos et al.,  
380 2021; van Dam et al., 2007). Additionally, agreement is poor for sites located in the vicinity of the  
381 Parkfield segment (specific regions across the fault perform poorly), which is consistent with the  
382 disagreement shown in Fig. 3.

383



384

385 Figure 4: Variance reduction between GPS and GRACE(-FO) vertical displacements

386

387 We also compared the annual amplitudes of GPS and GRACE(-FO) vertical displacements (cosine and  
388 sine components in Eq. 2). This analysis was not informative for the presence of outliers or errors in the  
389 current data sample studied.

390

391 Overall, the screening process not only assisted in outlier detection, but it also allowed for a deeper look  
392 into the structure of vertical displacement periodic signals. We identified the need for antenna offset  
393 corrections (in sites located in the Great Lakes region); removed sites affected by glacial isostatic  
394 adjustment and interseismic modeling errors; and sites located at the Parkfield segment of San Andreas  
395 Fault.

396

### 397 3. Uncertainty Quantification

398

399 With the updated [dataset](#) we are now ready to proceed with the uncertainty quantification of the GPS  
400 vertical displacement timeseries. We apply different error characterization schemes consisting of a root  
401 sum square of a random error, white noise error, power law noise error (flicker noise and random walk)  
402 and spatially coherent error.

403

#### 404 3.1 Methods

405

##### 406 *Root Mean Square Error*

407

408 Residuals  $r$  of a series with respect to a trajectory model (Eq. 2) are often used as a first approximation of  
409 noise in vertical displacement series (e.g., Bos et al., 2013; Michel et al., 2021). Practically,  $r$  shows how  
410 well a trajectory model can describe the original [timeseries](#). Therefore, the root mean square (rms) of  $r$   
411 can give a first approximation of the noise floor of each station.

412

##### 413 *Spectral Analysis, White, Flicker and Random Walk Noise*

414

415 Power distribution of residuals and its agreement with noise models, is another popular way to quantify  
416 uncertainty of GPS [timeseries](#) (e.g., Klos et al., 2019; Argus et al., 2022). Typically, GPS series are  
417 evaluated for white, flicker and random walk noise, or combination of them. Hector software (Bos et al.,  
418 2013) is used to estimate full noise covariance information by means of a maximum likelihood estimator.  
419 The covariance matrix  $C$  from a combination of white and power law (i.e., flicker and random walk) noise  
420 is given as:

421

$$C = a \times I + b \times J \quad \text{Eq. 4}$$

422

423 Where  $a$  is the amplitude of white noise,  $I$  is the identity matrix of size  $N$  (number of samples/epochs in  
424 the series),  $b$  is the amplitude and  $J$  the covariance matrix of power law noise.  $J$  matrix is a full  
425 covariance matrix that describes the time-correlated error (as the data record length increases, the  
426 displacement uncertainty changes (Bos et al., 2008 Eqs. 8-11)). The optimal selection of the noise models  
427 is done via two optimality criteria, namely the Akaike Information Criterion (Akaike, 1974) and the  
428 Bayesian Criterion (Schwarz, 1978).

429

430 In this study, we consider three cases:

431 a) White Noise (WN)

432 b) Combination of WN and Flicker Noise (WN+FN)

433 c) Combination of WN, FN and Random Walk Noise (WN+FN+RW)

434 We take the root-sum-squares of the noise magnitudes as our noise floor. For example, for the case of

435 WN+FN noise, noise is derived as  $\sigma = \pm \sqrt{\sigma_{WN}^2 + \sigma_{FN}^2}$ . Our data are sampled on a monthly basis, thus

Deleted: data set

Deleted: time-series

Deleted: time-series

439  $\sigma_{FN}$  needs to be scaled appropriately, i.e.,  $\sigma_{FN} = \sigma_{PL} \left(\frac{1}{12}\right)^{-\frac{k}{4}}$ , where,  $\sigma_{PL}$  is the uncertainty of power-law  
 440 (PL) and  $k$  the spectral index, outputted from Hector (more information on power-law noise estimation  
 441 can be found in Bos et al., 2008, and Williams, 2003).

442  
 443 *Common Mode Noise*  
 444

445 The Common Mode Component (CMC) is derived following the processing scheme suggested by  
 446 Kreemer and Blewitt (2021), which can be summarized as:

- 447  
 448 1) Input GPS displacement ~~timeseries~~ (referenced to Sep 2012) for  $j$  stations ( $l_j$ )  
 449 2) Derive each station's residuals by removing the trajectory part of the series ( $l_j(t) - y_j(t)$ )  
 450 3) Quantify the correlation coefficient  $r_{MAD}$  using robust statistics.  $r_{MAD}$  is defined as:

$$r_{MAD} = \frac{MAD^2(u) - MAD^2(v)}{MAD^2(u) + MAD^2(v)} \quad \text{Eq. 5}$$

451  
 452 The median absolute deviation ( $MAD$ ) is the absolute deviation around the median. For example, for a  
 453 residual series  $res(t)$   $MAD = |res(t) - median(res(t))|$ .  $u$  and  $v$  are derived as:

$$u = \frac{p - median(p)}{\sqrt{2}MAD(p)} + \frac{q - median(q)}{\sqrt{2}MAD(q)} \quad \text{Eq. 6}$$

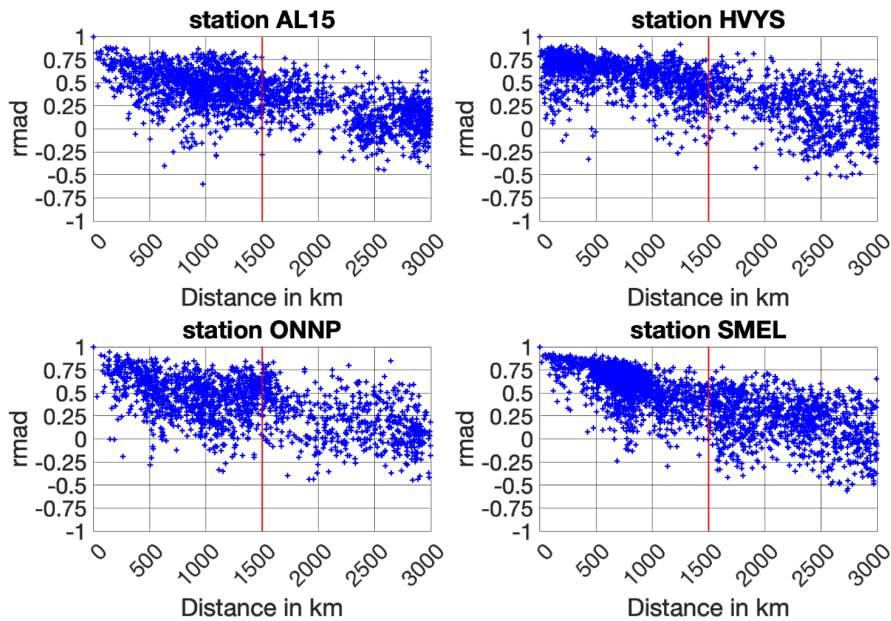
$$v = \frac{p - median(p)}{\sqrt{2}MAD(p)} - \frac{q - median(q)}{\sqrt{2}MAD(q)} \quad \text{Eq. 7}$$

454  
 455 with  $p$  and  $q$  being the residual series of the reference station and the neighbor station, respectively.  
 456 For each station there are  $j - 1$  correlation coefficients  $r_{MAD}$ . In order to decide the cut-off distance  
 457 that a neighbor station will be considered in the analysis we plot  $r_{MAD}$  coefficient against its distance  
 458 from the reference station (Fig. 5). Based on results from all stations we decide to set a cut-off at 1500  
 459 km, slightly higher than the 1350 km suggested by Kreemer and Blewitt (2021). The 1500 km cut-off  
 460 allows us to separate stations between East and West coast, as spatially coherent signals at stations  
 461 located across the continent are negligible.

- 462 4) Derive the median slope estimator ( $ccs$ ) using Theil-Sen median trend.  $ccs$  is the median trend of the  
 463  $r_{MAD}$  coefficients of a station against their distance with the reference station.  
 464 5) Derive the zero-distance intercept  $cci_j$  for each station as  $median(r_{MAD} - ccs * d)$ , with  $d$  being the  
 465 distance between the station of reference and the neighbor station (maximum  $d = 1500$  km).

Deleted: time-series

467 6) Construct CMC: Calculate the cumulative ( $c_j$ ) and percentile ( $p_j$ ) weights for each station and then  
 468 find the weighted median that corresponds to  $p_j = 50\%$ . This weighted median represents the CMC of  
 469 the station (Fig. 6).



470 Figure 5:  $r_{MAD}$  coefficient of four random stations with the rest of the station sample, plotted against the  
 471 distance of the reference station with the rest of the stations. Each cross resembles the  $r_{MAD}$  of the  
 472 reference station with a station located at distance  $d$ .  
 473  
 474

475 CMC is limited in providing a realistic error approximation, in that the technique cannot isolate spatially  
 476 correlated noise from signal (e.g., hydrology signals not described by the trajectory model are present in  
 477 the residuals fed into CMC). Under the realistic assumption that a component of the high frequency signal  
 478 contained in CMC reflects real hydrological processes, we remove the contribution of surface hydrology  
 479 using Global Land Data Assimilation System (GLDAS) (Rodell et al., 2004) vertical displacement  
 480 estimates. GLDAS does not model deep groundwater and open surface water, so these signals remain in  
 481 the residual (Scanlon et al., 2018). Vertical displacement estimates driven by surface hydrology are  
 482 derived similar to GRACE(-FO) (Section 2.2). We use Noah v2.1 monthly estimates of soil moisture  
 483 storage given at 0.25-degree grids (Beaudoing and Rodell, 2016), convert the fields from terrestrial water  
 484 storage ( $\text{kg}/\text{m}^2$ ) to units of equivalent water height, derive the spherical harmonic coefficients of the  
 485 equivalent water height mass load using Wahr et al. (1998), and predict the elastic response of the Earth  
 486 (Eq. 1). Afterwards, we remove the reference epoch (09/2012) similar to GPS and estimate the vertical  
 487 displacement at the locations of the GPS sites by interpolating the estimates of the closest neighbors to the  
 488 station's location. Note, that because our interest is to prepare the data for a combined solution with  
 489 GRACE(-FO) we interpolate the timeseries at the times of GRACE(-FO) monthly series availability. The

Deleted: up displacement

491 interested reader is referred to the supplement, where we show the vertical displacement estimated by  
 492 GPS, GRACE(-FO) and GLDAS (Figure S2) for randomly selected stations. Finally, we derive residuals  
 493 relative to the trajectory model (Eq. 2). GLDAS (surface hydrology) residuals should ideally reflect high  
 494 frequency hydrological processes and are therefore removed from GPS residuals. Overall, CMC of  
 495 surface hydrology residuals exhibits a fairly small magnitude (~0.5 mm). We remove the contribution of  
 496 surface hydrology within the CMC algorithm by first subtracting GLDAS vertical displacement estimates  
 497 from GPS, and next inputting the residuals of this difference into the algorithm. The output of this process  
 498 (CMC<sub>HF</sub>) slightly decreases the magnitude of CMC and expresses a more realistic representation of  
 499 spatially correlated noise.

Deleted: up displacement

### 501 3.2 Results

502  
 503 Vertical displacement uncertainty of each station is estimated by means of all the different approaches  
 504 discussed in Section 3. Mean ( $\mu$ ), median and standard deviation (std) values are shown in Table 1. On  
 505 average, an assumption of white noise shows slightly reduced uncertainty compared to the other  
 506 techniques, followed by RMSE. When flicker noise is considered in addition to white noise (WN+FN) the  
 507 average uncertainty increases by nearly 0.8 mm compared to the white noise only. We note that the  
 508 contribution of white noise in the case of WN+FN is negligible for ninety seven percent of the stations  
 509 (that is flicker noise describes the noise exclusively). Noise level from combination of all three noise  
 510 models (WN+FN+RW) is less than 4 mm on average. In this case too, white noise is negligible, and noise  
 511 is described exclusively from flicker noise for 1550 stations, and from random walk for 600 stations. The  
 512 rest of the data sample reflects a contribution from both noise models. We additionally analyzed the  
 513 amplitude of the noise of each noise model ( $\sigma_{PL}$ ) with respect to the length of the input series. Results did  
 514 not identify any clear relationship between  $\sigma_{PL}$  and the length of each station's timeseries. CMC noise  
 515 floor is 3.6 mm on average with a relatively large standard deviation ( $\pm 1.6$  mm) which suggests that  
 516 spatially correlated noise has higher variability than time-correlated noise ( $\pm 1.6$  mm as opposed to  $\sim \pm 1$   
 517 mm). When surface hydrology is removed (CMC<sub>HF</sub>) the noise floor drops by a fraction of a mm on  
 518 average compared to CMC.

519  
 520 Table 1: Different uncertainty quantification cases

	mean ( $\mu$ ) (mm)	median (mm)	$\pm$ std (mm)
RMSE	2.8	2.7	0.8
WN	2.4	2.2	0.8
WN+FN	3.2	3.1	0.7
WN+FN+RW	3.8	3.5	1.1
CMC	3.6	3.2	1.6
CMC <sub>HF</sub>	3.5	3.1	1.6

521  
 522 RMSE and WN exhibit a smooth transition among the regions, which indicates the presence of spatially  
 523 coherent regime signal mostly driven by hydrology (Fig. 6). The combination of WN+FN is mostly  
 524 dominated by FN and the uncertainty exhibits local (in space) coherence. The uncertainty is larger when

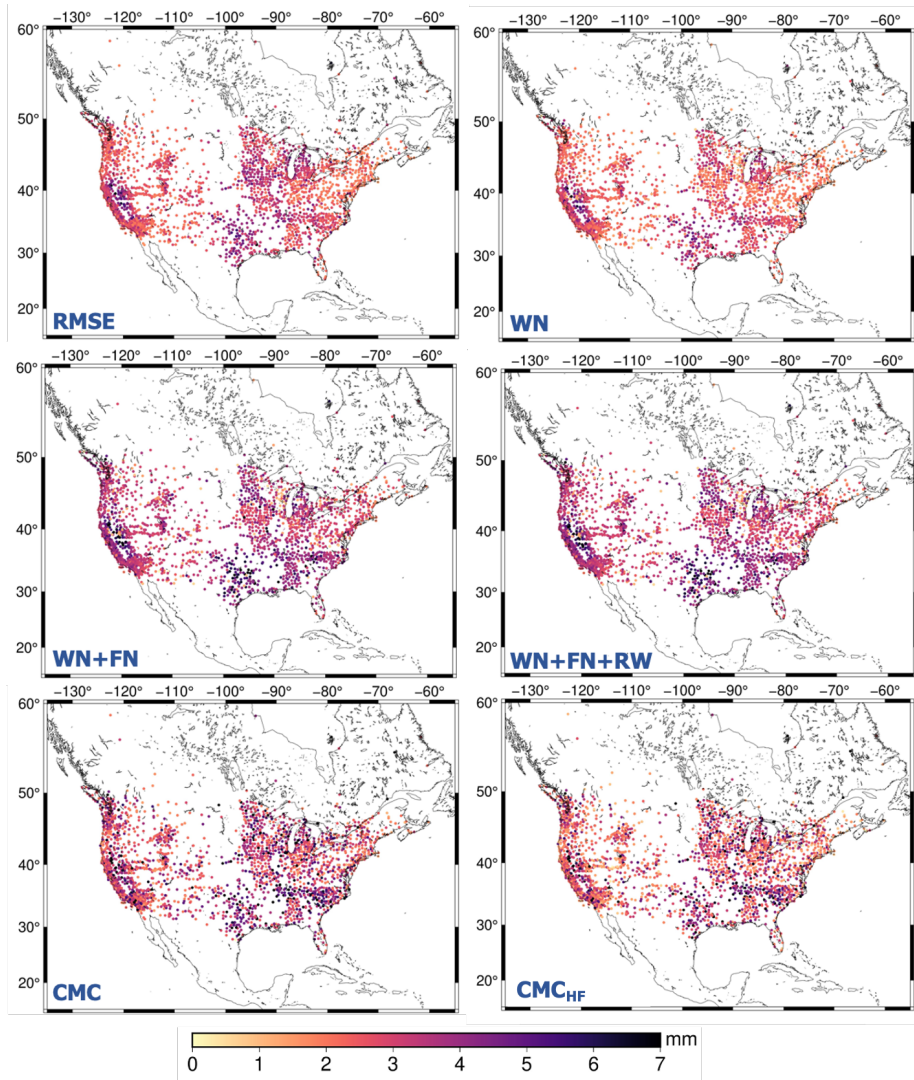
526 random walk is included in the combination (WN+FN+RW). A recent study from Argus et al. (2022) on  
527 groundwater flux in Central Valley (California) suggests that noise on GPS-derived uplift motion can be  
528 well described by a combination of flicker noise and random walk, due to the ability of these noise  
529 models to reflect low frequency noise. When a simulated contribution of the surface hydrological  
530 component is removed from the series,  $CMC_{HF}$  reflects a more realistic picture of the noise. Arguably the  
531 level of change compared to CMC is sub-millimeter. Signal contributions from un-modelled groundwater  
532 variations are potentially still present, but groundwater changes are typically slower in time.

533  
534  
535 We obtain the relative likelihood of each uncertainty quantification method by estimating the probability  
536 density function (PDF) (Fig. 7). White noise has a flat power spectrum, having the same amplitude  
537 across frequencies. Estimating a best fit for a flat spectrum doesn't allow for capturing the long tail skew  
538 of the residuals (low frequency), which are biased towards their mean. Thus, the amplitude of white noise  
539 is smaller compared to the rest of the techniques (Table 1). Flicker and random walk noise models add to  
540 the long tail of the power distribution, that is they allow more low frequency noise, which explains the  
541 higher amplitude of the uncertainty when these two noise types are considered.

542 RMSE and WN show a 50% probability of a station having an uncertainty ( $\sigma$ ) between 1.5-2 mm and less  
543 than 10% of a station exceeding  $\sigma=4$  mm. The noise level falls within [2 4] mm for ~93% of the stations  
544 when we consider combination of WN+FN. PDF of RMSE, WN and WN+FN resemble a normal  
545 distribution, with the mean being shifted for each case. When random walk is also considered  
546 (WN+FN+RW) 64% of the stations exhibit noise within [2 4] mm. In this case, the distribution is more  
547 spread resembling a gamma-like distribution, with a peak being at 3 mm (18%). CMC and  $CMC_{HF}$  PDF  
548 also follow a gamma-shape, and the probability of the uncertainty ranging between [2 4] mm is nearly  
549 60% for CMC and 65% when surface hydrology is removed.

550





551  
552  
553

Figure 6: Noise amplitudes of GPS timeseries estimated using different techniques.

Deleted: Uncertainty

Deleted: various

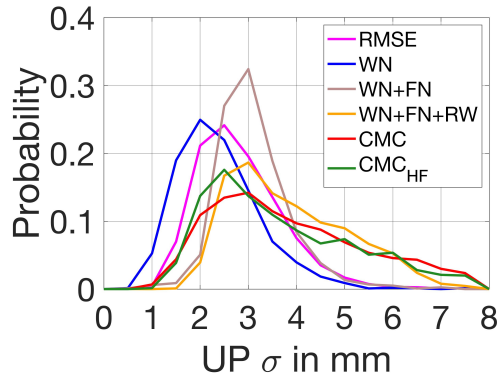


Figure 7: Probability density function of vertical displacement estimates uncertainty

556  
557

558

#### 559 **4. Discussion and Conclusions**

560

561 GPS-derived vertical displacements are very useful for supplementing GRACE(-FO) gravity products to  
 562 infer mass change signals at spatial scales smaller than what can typically be achieved with current  
 563 satellite gravimetry alone (i.e., < 300km). This work provides a general workflow to isolate elastic surface  
 564 mass signals from GPS vertical displacement, by developing processing standards; additionally, it  
 565 suggests uncertainty quantification schemes to quantify error on GPS vertical displacement estimates. The  
 566 ultimate goal is to prepare GPS estimates for merging with satellite-gravimetry observations. First, we  
 567 provide a list of corrections needed for isolating surface mass following recommendations outlined in  
 568 Argus et al. (2017; 2022). Additionally, a detailed investigation of trends, correlation, and variance  
 569 reduction highlights the need for better background modeling (glacial isostatic adjustment and  
 570 interseismic strain), as the two observation techniques respond differently in the presence of such errors.  
 571 At this point the recommendation is to remove sites located in the vicinity of regions where background  
 572 models are known to perform poorly, before any joint inversion. Except detecting outlier stations,  
 573 screening metrics point to extra corrections that need to be applied in certain sites (e.g., missed antenna  
 574 offsets).

575 Several uncertainty quantification schemes have been tested to prescribe weights on GPS vertical  
 576 displacement estimates that are needed for a joint inversion with GRACE(-FO) data. The average noise  
 577 level indicated by RMSE is 2.8 mm. White noise average is 2.5 mm. The errors increase when lower  
 578 frequencies are included in the noise estimation. When we account for flicker noise, one third of the sites  
 579 exhibits noise levels of up to 3 mm. The average noise increases significantly in presence of random  
 580 walk, as more power of the lower frequencies gets into the estimations, and the distribution of noise is  
 581 more dispersed. In this case, half of the stations are prescribed with > 4 mm uncertainty. Argus et al.  
 582 (2022), finds that random walk is the most realistic representation of noise based on postfit residuals. We  
 583 notice that the spectrum of CMC provides similar uncertainties to random walk, which implies that  
 584 despite the different characterization procedure, CMC is able to provide equally realistic noise estimates  
 585 of GPS timeseries. We attempted to minimize lingering hydrology signals embedded in CMC, through

586 reducing the GPS vertical displacement observations with displacements from the GLDAS hydrology  
587 model. The average noise floor dropped slightly (~0.5 mm drop in sigma). Future work will provide  
588 further information of GPS station errors when the weight of each GPS site is also considered based on its  
589 impact on the performance in a formal data combination of GPS-GRACE(-FO). The suggested  
590 framework can be easily adjusted to account for global ~~datasets~~. The new ~~dataset~~ provides GPS vertical  
591 displacements of elastic mass variations in North America and their associated uncertainties.  
592

Deleted: data set

Deleted: data set

593 **Data Availability:** The data product described in the manuscript is available in zenodo (doi:  
594 <https://zenodo.org/record/8184285>). GPS timeseries are provided by the Global Station List from the  
595 Nevada Geodetic Laboratory (<http://geodesy.unr.edu/>; Blewitt et al., 2018). Non atmospheric and oceanic  
596 tidal aliasing product (AOD1B RL06) is provided by GFZ's Information System and Data Center  
597 (<ftp://isdg.gfz-potsdam.de/grace/Level-1B/GFZ/AOD/RL06>, Dobslaw et al., 2017). GRACE and  
598 GRACE-FO Level 2 products are available from podaac (<https://doi.org/10.5067/GFL20-MJ060>).  
599

600 **Acknowledgments:** The research was carried out at the Jet Propulsion Laboratory, California Institute  
601 of Technology, under a contract with the National Aeronautics and Space Administration  
602 (80NM0018D0004). Maps were made with the Generic Mapping Toolbox (Wessel et al. 2019). *We thank*  
603 *Corne Kreemer (UNR) for his feedback and Mike Heflin (JPL) for his insights on draconitic errors.*  
604

## 605 References

606 Akaike, H.: A new look at the statistical model identification. IEEE transactions on automatic control,  
607 19(6), pp.716-723. <https://doi.org/10.1109/TAC.1974.1100705>, 1974.  
608

609 Altamimi, Z., Rebischung, P., Métivier, L. and Collilieux, X.: ITRF2014: A new release of the  
610 International Terrestrial Reference Frame modeling nonlinear station motions. Journal of Geophysical  
611 Research: Solid Earth, 121(8), pp.6109-6131. <https://doi.org/10.1002/2016JB013098>, 2016.  
612

613 Amiri-Simkooei, A.R., Mohammadloo, T.H. and Argus, D.F.: Multivariate analysis of GPS position  
614 ~~timeseries~~ of JPL second reprocessing campaign. Journal of Geodesy, 91, pp.685-704.  
615 <https://doi.org/10.1007/s00190-016-0991-9>, 2017.  
616

Deleted: time series

617 Argus, D.F., Fu, Y. and Landerer, F.W.: Seasonal variation in total water storage in California inferred  
618 from GPS observations of vertical land motion. Geophysical Research Letters, 41(6), pp.1971-1980.  
619 <https://doi.org/10.1002/2014GL059570>, 2014.  
620

621 Argus, D.F., Gordon, R.G., Heflin, M.B., Ma, C., Eanes, R.J., Willis, P., Peltier, W.R. and Owen, S.E.:  
622 The angular velocities of the plates and the velocity of Earth's centre from space geodesy. Geophysical  
623 Journal International, 180(3), pp.913-960. <https://doi.org/10.1111/j.1365-246X.2009.04463.x>, 2010.  
624

625 Argus, D.F., Landerer, F.W., Wiese, D.N., Martens, H.R., Fu, Y., Famiglietti, J.S., Thomas, B.F., Farr,  
626 T.G., Moore, A.W. and Watkins, M.M.: Sustained water loss in California's mountain ranges during  
627 severe drought from 2012 to 2015 inferred from GPS. Journal of Geophysical Research: Solid Earth,  
628 122(12), pp.10-559. <https://doi.org/10.1002/2017JB014424>, 2017.  
629

633  
634 Argus, D. F., Peltier, W. R., Drummond, R. and Moore, A. W.: The Antarctica component of postglacial  
635 rebound model ICE-6G\_C (VM5a) based on GPS positioning, exposure age dating of ice thicknesses, and  
636 relative sea level histories. *Geophysical Journal International*, 198, 537–563.  
637 <https://doi.org/10.1093/gji/ggu140>, 2014.  
638  
639 Argus, D.F., Martens, H.R., Borsa, A.A., Knappé, E., Wiese, D.N., Alam, S., Anderson, M., Khatiwada,  
640 A., Lau, N., Peidou, A. and Swarr, M.: Subsurface water flux in California's Central Valley and its source  
641 watershed from space geodesy. *Geophysical Research Letters*, 49(22), p.e2022GL099583.  
642 <https://doi.org/10.1029/2022GL099583>, 2022.  
643  
644 Argus, D.F., Peltier, W.R., Blewitt, G. and Kreemer, C.: The Viscosity of the Top Third of the Lower  
645 Mantle Estimated Using GPS, GRACE, and Relative Sea Level Measurements of Glacial Isostatic  
646 Adjustment. *Journal of Geophysical Research: Solid Earth*, 126(5), p.e2020JB021537.  
647 <https://doi.org/10.1029/2020JB021537>, 2021.  
648  
649 Beaudoin, H. and M. Rodell: GLDAS Noah Land Surface Model L4 monthly 0.25 x 0.25 degree V2.1,  
650 Greenbelt, Maryland, USA, Goddard Earth Sciences Data and Information Services Center (GES DISC).  
651 <https://doi.org/10.5067/SXAVCZFAQLNO>, 2020.  
652  
653 Becker, J.M. and Bevis, M.: Love's problem. *Geophysical Journal International*, 156(2), pp.171-178.  
654 <https://doi.org/10.1111/j.1365-246X.2003.02150.x>, 2004.  
655  
656 Bertiger, W., Bar-Sever, Y., Dorsey, A., Haines, B., Harvey, N., Hemberger, D., Heflin, M., Lu, W.,  
657 Miller, M., Moore, A.W. and Murphy, D.: GipsyX/RTGx, a new tool set for space geodetic operations  
658 and research. *Advances in space research*, 66(3), pp.469-489. <https://doi.org/10.1016/j.asr.2020.04.015>,  
659 2020.  
660  
661 Bevis, M. and Brown, A.: Trajectory models and reference frames for crustal motion geodesy (2014).  
662 *Journal of Geodesy*, 88, 283–311, doi: 10.1007/s00190-013-0685-5.  
663  
664 Blewitt, G., Hammond, W.C. and Kreemer, C.: Harnessing the GPS data explosion for interdisciplinary  
665 science. *Eos*, 99(10.1029), p.485. doi.org/10.1029/2018EO104623.  
666 <https://doi.org/10.1029/2018EO104623>, 2018.  
667  
668 Blewitt, G., Lavallée, D., Clarke, P. and Nurutdinov, K.: A new global mode of Earth deformation:  
669 Seasonal cycle detected. *Science*, 294(5550), pp.2342-2345.  
670 <https://doi.org/10.1126/science.1065328>, 2001.  
671  
672 Boehm, J., Werl, B., and Schuh, H.: Troposphere mapping functions for GPS and very long baseline  
673 interferometry from European Centre for Medium-Range Weather Forecasts operational analysis data. *J.*  
674 *Geophys. Res.*, 111, B02406, doi:[10.1029/2005JB003629](https://doi.org/10.1029/2005JB003629), 2006.  
675

676 Borsa, A.A., Agnew, D.C. and Cayan, D.R.: December. Drought-induced uplift in the western United  
677 States as observed by the EarthScope Plate Boundary Observatory GPS network. In AGU Fall Meeting  
678 Abstracts (Vol. 2014, pp. G23B-0481), 2014.  
679  
680 Bos, M.S., Fernandes, R.M.S., Williams, S.D.P. and Bastos, L.: Fast error analysis of continuous GPS  
681 observations. *Journal of Geodesy*, 82(3), pp.157-166. <https://doi.org/10.1007/s00190-007-0165-x>, 2008.  
682  
683 Bos, M.S., Fernandes, R.M.S., Williams, S.D.P. and Bastos, L.: Fast error analysis of continuous GPS  
684 observations with missing data. *Journal of Geodesy*, 87(4), pp.351-360. <https://doi.org/10.1007/s00190-012-0605-0>, 2013.  
685  
686  
687 Chew, C.C. and Small, E.E.: Terrestrial water storage response to the 2012 drought estimated from GPS  
688 vertical position anomalies. *Geophysical Research Letters*, 41(17), pp.6145-6151.  
689 <https://doi.org/10.1002/2014GL061206>, 2014.  
690  
691 Crowell, B.W., Bock, Y. and Liu, Z.: Single-station automated detection of transient deformation in GPS  
692 ~~timeseries~~ with the relative strength index: A case study of Cascadian slow slip. *Journal of Geophysical*  
693 *Research: Solid Earth*, 121(12), pp.9077-9094. <https://doi.org/10.1002/2016JB013542>, 2016.  
694  
695 Davis, J.L., Elósegui, P., Mitrovica, J.X. and Tamisiea, M.E.: Climate-driven deformation of the solid  
696 Earth from GRACE and GPS. *Geophysical Research Letters*, 31(24).  
697 <https://doi.org/10.1029/2004GL021435>, 2004.  
698  
699 Dee, D.P., Uppala, S.M., Simmons, A.J., Berrisford, P., Poli, P., Kobayashi, S., Andrae, U., Balmaseda,  
700 M.A., Balsamo, G., Bauer, D.P. and Bechtold, P.: The ERA-Interim reanalysis: Configuration and  
701 performance of the data assimilation system. *Quarterly Journal of the royal meteorological society*,  
702 137(656), pp.553-597. <https://doi.org/10.1002/qj.828>, 2011.  
703  
704 Dill, R., and Dobsław, H.: Numerical simulations of global-scale high resolution hydrological crustal  
705 deformations. *Journal of Geophysical Research: Solid Earth*, 118(9), 5008–5017.  
706 <https://doi.org/10.1002/jgrb.50353>, 2013.  
707  
708 Dobsław, H., Bergmann-Wolf, I., Dill, R., Poropat, L., Thomas, M., Dahle, C., Esselborn, S., König, R.  
709 and Flechtner, F.: A new high-resolution model of non-tidal atmosphere and ocean mass variability for  
710 de-aliasing of satellite gravity observations: AOD1B RL06. *Geophysical Journal International*, 211(1),  
711 pp.263-269. <https://doi.org/10.1093/gji/ggx302>, 2017.  
712  
713 Dong, D., Fang, P., Bock, Y., Webb, F., Prawirodirdjo, L., Kedar, S., and Jamason, P.: Spatiotemporal  
714 filtering using principal component analysis and Karhunen-Loeve expansion approaches for regional GPS  
715 network analysis, *J. Geophys. Res.*, 111, B03405, <https://doi.org/10.1029/2005JB003806>, 2006.  
716  
717 Frederikse, T., Landerer, F., Caron, L., Adhikari, S., Parkes, D., Humphrey, V.W., Dangendorf, S.,  
718 Hogarth, P., Zanna, L., Cheng, L. and Wu, Y.H.: The causes of sea-level rise since 1900. *Nature*,  
719 584(7821), pp.393-397. <https://doi.org/10.1038/s41586-020-2591-3>, 2020.

Deleted: time series

721 Fu, Y. and Freymueller, J.T.: Seasonal and long-term vertical deformation in the Nepal Himalaya  
722 constrained by GPS and GRACE measurements. *Journal of Geophysical Research: Solid Earth*, 117(B3).  
723 <https://doi.org/10.1029/2011JB008925>, 2012.  
724  
725  
726 Fu, Y., Argus, D.F. and Landerer, F.W.: GPS as an independent measurement to estimate terrestrial water  
727 storage variations in Washington and Oregon. *Journal of Geophysical Research: Solid Earth*, 120(1),  
728 pp.552-566. <https://doi.org/10.1002/2014JB011415>, 2015.  
729  
730 Fukumori, I., Wang, O., Llovel, W., Fenty, I. and Forget, G.: A near-uniform fluctuation of ocean bottom  
731 pressure and sea level across the deep ocean basins of the Arctic Ocean and the Nordic Seas. *Progress in*  
732 *Oceanography*, 134, pp.152-172. <https://doi.org/10.1016/j.pocean.2015.01.013>, 2015.  
733  
734 Gazeaux, J., Williams, S., King, M., Bos, M., Dach, R., Deo, M., Moore, A.W., Ostini, L., Petrie, E.,  
735 Roggero, M. and Teferle, F.N.: Detecting offsets in GPS **timeseries**: First results from the detection of  
736 offsets in GPS experiment. *Journal of Geophysical Research: Solid Earth*, 118(5), pp.2397-2407.  
737 <https://doi.org/10.1002/jgrb.50152>, 2013.  
738  
739 Haines, B., Bar-Sever, Y., Bertiger, W., Desai, S. and Willis, P. One-centimeter orbit determination for  
740 Jason-1: new GPS-based strategies. *Marine Geodesy*, 27(1-2), pp.299-318.  
741 <https://doi.org/10.1007/BF03321179>, 2004.  
742  
743 Hammond, W. C., Blewitt, G., and Kreemer, C.: GPS Imaging of vertical land motion in California and  
744 Nevada: Implications for Sierra Nevada uplift, *J. Geophys. Res. Solid Earth*, 121, 7681–7703,  
745 doi:[10.1002/2016JB013458](https://doi.org/10.1002/2016JB013458), 2016.  
746  
747 He, X., Bos, M.S., Montillet, J.P. and Fernandes, R.M.S.: Investigation of the noise properties at low  
748 frequencies in long GPS **timeseries**. *Journal of Geodesy*, 93(9), pp.1271-1282.  
749 <https://doi.org/10.1007/s00190-019-01244-y>, 2019.  
750  
751 Houborg, R., Rodell, M., Li, B., Reichle, R. and Zaitchik, B.F.: Drought indicators based on model-  
752 assimilated Gravity Recovery and Climate Experiment (GRACE) terrestrial water storage observations.  
753 *Water Resources Research*, 48(7). <https://doi.org/10.1029/2011WR011291>, 2012.  
754  
755 Ji, K.H. and Herring, T.A. A method for detecting transient signals in GPS position **timeseries**: smoothing  
756 and principal component analysis. *Geophysical Journal International*, 193(1), pp.171-186.  
757 <https://doi.org/10.1093/gji/ggt003>, 2013.  
758  
759 Jiang, W., Li, Z., van Dam, T. and Ding, W.: Comparative analysis of different environmental loading  
760 methods and their impacts on the GPS height **timeseries**. *Journal of Geodesy*, 87(7), pp.687-703.  
761 <https://doi.org/10.1007/s00190-013-0642-3>, 2013.  
762

Deleted: time series

Deleted: time series

Deleted: time-series

Deleted: time series

767 Klos, A., Bogusz, J., Figurski, M. and Kosek, W.: Uncertainties of geodetic velocities from permanent  
768 GPS observations: the Sudeten case study. *Acta Geodynamica et Geomaterialia*, 11(3), p.175.  
769 <https://doi.org/10.13168/AGG.2014.0005>, 2014.  
770

771 Klos, A., Dobsław, H., Dill, R. and Bogusz, J.: Identifying the sensitivity of GPS to non-tidal loadings at  
772 various time resolutions: examining vertical displacements from continental Eurasia. *GPS Solutions*,  
773 25(3), p.89. <https://doi.org/10.1007/s10291-021-01135-w>, 2021.  
774

775 Klos, A., Kusche, J., Fenoglio-Marc, L., Bos, M.S. and Bogusz, J.: Introducing a vertical land  
776 displacement model for improving estimates of sea level rates derived from tide gauge records affected by  
777 earthquakes. *GPS Solutions*, 23(4), pp.1-12. <https://doi.org/10.1007/s10291-019-0896-1>, 2019.  
778

779 [Klos, A., Kusche, J., Leszczuk, G., Gerdener, H., Schulze, K., Lenczuk, A. and Bogusz, J.: Introducing](#)  
780 [the Idea of Classifying Sets of Permanent GNSS Stations as Benchmarks for Hydrogeodesy. \*Journal of\*](#)  
781 [\*Geophysical Research: Solid Earth\*, 128\(9\), p.e2023JB026988. <https://doi.org/10.1029/2023JB026988>,](#)  
782 [2023.](#)  
783

784 Kreemer, C. and Blewitt, G.: Robust estimation of spatially varying common-mode components in GPS  
785 [time series](#). *Journal of geodesy*, 95(1), pp.1-19. <https://doi.org/10.1007/s00190-020-01466-5>, 2021.  
786

787 Kumar, U., Chao, B.F. and Chang, E.T.: What causes the common-mode error in array GPS displacement  
788 fields: Case study for Taiwan in relation to atmospheric mass loading. *Earth and Space Science*, 7(11),  
789 p.e2020EA001159. <https://doi.org/10.1029/2020EA001159>, 2020.  
790

791 Landerer, F.W., Flechtner, F.M., Save, H., Webb, F.H., Bandikova, T., Bertiger, W.I., Bettadpur, S.V.,  
792 Byun, S.H., Dahle, C., Dobsław, H. and Fahnestock, E.: Extending the global mass change data record:  
793 GRACE Follow-On instrument and science data performance. *Geophysical Research Letters*, 47(12),  
794 p.e2020GL088306. <https://doi.org/10.1029/2020GL088306>, 2020.  
795

796 Li, S., Wang, K., Wang, Y., Jiang, Y. and Dosso, S.E.: Geodetically inferred locking state of the Cascadia  
797 megathrust based on a viscoelastic Earth model. *Journal of Geophysical Research: Solid Earth*, 123(9),  
798 pp.8056-8072. <https://doi.org/10.1029/2018JB015620>, 2018.  
799

800 Li, W. and Shen, Y.: The consideration of formal errors in spatiotemporal filtering using principal  
801 component analysis for regional GPS position [time series](#). *Remote Sensing*, 10(4), p.534.  
802 <https://doi.org/10.3390/rs10040534>, 2018.  
803

804 Liu, B., Dai, W., Peng, W. and Meng, X.: Spatiotemporal analysis of GPS [time series](#) in vertical direction  
805 using independent component analysis. *Earth, Planets and Space*, 67(1), pp.1-10.  
806 <https://doi.org/10.1186/s40623-015-0357-1>, 2015.  
807

808 Loomis, B.D., Rachlin, K.E. and Luthcke, S.B.: Improved Earth oblateness rate reveals increased ice  
809 sheet losses and mass-driven sea level rise. *Geophysical Research Letters*, 46(12), pp.6910-6917.  
810 <https://doi.org/10.1029/2019GL082929>, 2019.  
811

Formatted: Font: 11 pt

Formatted: Line spacing: single

Formatted: Font: 11 pt

Formatted: Font: 11 pt

Deleted: time-series

Deleted: time series

Deleted: time series



815 Martens, H. R., Argus, D. F., Norberg, C., Blewitt, G., Herring, T. A., Moore, A. W., et al.: Atmospheric  
816 pressure loading in GPS positions: Dependency on GPS processing methods and effect on assessment of  
817 seasonal deformation in the contiguous USA and Alaska. *Journal of*  
818 *Geodynamics*, 94(12), 115, <https://doi.org/10.1007/s00190-020-01445-w>, 2020.

819  
820 Michel, A., Santamaría-Gómez, A., Boy, J.P., Perosanz, F. and Loyer, S.: Analysis of GPS Displacements  
821 in Europe and Their Comparison with Hydrological Loading Models. *Remote Sensing*, 13(22), p.4523.  
822 <https://doi.org/10.3390/rs13224523>, 2021.

823  
824 Milliner, C., Materna, K., Bürgmann, R., Fu, Y., Moore, A.W., Bekaert, D., Adhikari, S. and Argus, D.F.:  
825 Tracking the weight of Hurricane Harvey's stormwater using GPS data. *Science advances*, 4(9),  
826 p.eaa2477. <https://doi.org/10.1126/sciadv.aau2477>, 2018.

827  
828 Montillet, J.P., Melbourne, T.I. and Szeliga, W.M.: GPS vertical land displacement corrections to sea-  
829 level rise estimates in the Pacific Northwest. *Journal of Geophysical Research: Oceans*, 123(2), pp.1196-  
830 1212. <https://doi.org/10.1002/2017JC013257>, 2018.

831  
832 Nikolaidis, R.: Observation of geodetic and seismic deformation with the Global Positioning System.  
833 University of California, San Diego, 2002.

834  
835 Pail, R., Bingham, R., Braitenberg, C., Dobsław, H., Eicker, A., Güntner, A., Horwath, M., Ivins, E.,  
836 Longuevergne, L., Panet, I. and Wouters, B.: Science and user needs for observing global mass transport  
837 to understand global change and to benefit society. *Surveys in Geophysics*, 36(6), pp.743-772.  
838 <https://doi.org/10.1007/s10712-015-9348-9>, 2015.

839  
840 Peltier, W. R., Argus, D. F. and Drummond, R. :Space geodesy constrains ice age terminal deglaciation:  
841 The global ICE-6G\_C (VM5a) model. *Journal Geophysical Research: Solid Earth*, 120, 450–487.  
842 <https://doi.org/10.1002/2014JB011176>, 2015.

843  
844 Peltier, W. R., Argus, D. F., and Drummond, R.: Comment on the paper by Purcell et al. 2016 entitled 'An  
845 assessment of ICE-6G\_C (VM5a) glacial isostatic adjustment model (2018). *Journal Geophysical*  
846 *Research: Solid Earth*, 122, 2019-2028. <https://doi.org/10.1002/2016JB013844>, 2018.

847  
848 Luzum, B. and Petit, G. (2012). The IERS Conventions: Reference systems and new models. *Proceedings*  
849 *of the International Astronomical Union*, 10(H16), 227-228. <https://doi:10.1017/S1743921314005535>,  
850 2012.

851  
852 Ray, J., Altamimi, Z., Collilieux, X. and van Dam, T.: Anomalous harmonics in the spectra of GPS  
853 position estimates. *GPS solutions*, 12, pp.55-64. <https://doi.org/10.1007/s10291-007-0067-7>, 2008.

854  
855 Reager, J.T., Thomas, B.F. and Famiglietti, J.S.: River basin flood potential inferred using GRACE  
856 gravity observations at several months lead time. *Nature Geoscience*, 7(8), pp.588-592.  
857 <https://doi.org/10.1038/ngeo2203>, 2014.

858



859 Rodell, M., Houser, P.R., Jambor, U.E.A., Gottschalk, J., Mitchell, K., Meng, C.J., Arsenault, K.,  
860 Cosgrove, B., Radakovich, J., Bosilovich, M. and Entin, J.K.: The global land data assimilation system.  
861 Bulletin of the American Meteorological society, 85(3), pp.381-394.  
862 <https://doi.org/10.1175/BAMS-85-3-381>, 2004.  
863  
864 Rodriguez-Solano, C.J., Hugentobler, U., Steigenberger, P., Bloßfeld, M. and Fritsche, M.: Reducing the  
865 draconitic errors in GPS geodetic products. Journal of Geodesy, 88(6), pp.559-574.  
866 <https://doi.org/10.1007/s00190-014-0704-1>, 2014.  
867  
868 Rui, H., Beaudoin, H. and Loeser, C.: README document for NASA GLDAS version 2 data products.  
869 Goddard Earth Sciences Data and Information Services Center (GES DISC): Greenbelt, MD, USA, 2018.  
870  
871 Santamaria-Gomez, A., Gravelle, M., Collilieux, X., Guichard, M., Míguez, B.M., Tiphaneau, P. and  
872 Wöppelmann, G.: Mitigating the effects of vertical land displacement in tide gauge records using a state-  
873 of-the-art GPS velocity field. Global and Planetary Change, 98, pp.6-17.  
874 <https://doi.org/10.1016/j.gloplacha.2012.07.007>, 2012.  
875  
876 Schwarz, G.: Estimating the dimension of a model. Annals of statistics, 6(2), pp.461-464.  
877 <https://doi.org/10.1214/aos/1176344136>, 1978.  
878  
879 Serpelloni, E., Faccenna, C., Spada, G., Dong, D. and Williams, S.D.: Vertical GPS ground motion rates  
880 in the Euro-Mediterranean region: New evidence of velocity gradients at different spatial scales along the  
881 Nubia-Eurasia plate boundary. Journal of Geophysical Research: Solid Earth, 118(11), pp.6003-6024.  
882 <https://doi.org/10.1002/2013JB010102>, 2013.  
883  
884 Simmons, A., Uppala, S., Dee, D. and Kobayashi, S.: ERA-Interim: New ECMWF reanalysis products  
885 from 1989 onwards. ECMWF newsletter, 110, 25-35. <https://doi.org/10.21957/pocnex23c6>, 2007.  
886  
887 Sun, Y., Riva, R. and Ditmar, P.: Optimizing estimates of annual variations and trends in geocenter  
888 motion and J2 from a combination of GRACE data and geophysical models, J. Geophys. Res. Solid Earth,  
889 121, <https://doi.org/10.1002/2016JB013073>, 2016.  
890  
891 Tapley, B.D., Watkins, M.M., Flechtner, F., Reigber, C., Bettadpur, S., Rodell, M., Sasgen, I.,  
892 Famiglietti, J.S., Landerer, F.W., Chambers, D.P. and Reager, J.T.: Contributions of GRACE to  
893 understanding climate change. Nature climate change, 9(5), pp.358-369.  
894 <https://doi.org/10.1038/s41558-019-0456-2>, 2019.  
895  
896 Thomas, A.C., Reager, J.T., Famiglietti, J.S. and Rodell, M.: A GRACE-based water storage deficit  
897 approach for hydrological drought characterization. Geophysical Research Letters, 41(5), pp.1537-1545.  
898 <https://doi.org/10.1002/2014GL059323>, 2014.  
899  
900 Thomas, B.F., Famiglietti, J.S., Landerer, F.W., Wiese, D.N., Molotch, N.P. and Argus, D.F.:  
901 Groundwater drought index: Evaluation of California Central Valley groundwater drought. Remote  
902 Sensing of Environment, 198, pp.384-392. <https://doi.org/10.1016/j.rse.2017.06.026>, 2017.

903  
904 Tian, Y. and Shen, Z.K.: Extracting the regional common-mode component of GPS station position  
905 [timeseries](#) from dense continuous network. *Journal of Geophysical Research: Solid Earth*, 121(2),  
906 pp.1080-1096. <https://doi.org/10.1002/2015JB012253>, 2016.  
907  
908 Tregoning, P., Watson, C., Ramillien, G., McQueen, H. and Zhang, J.: Detecting hydrologic deformation  
909 using GRACE and GPS. *Geophysical Research Letters*, 36(15). <https://doi.org/10.1029/2009GL038718>,  
910 2009.  
911  
912 Tsai, V.C.: A model for seasonal changes in GPS positions and seismic wave speeds due to thermoelastic  
913 and hydrologic variations. *Journal of Geophysical Research: Solid Earth*, 116(B4).  
914 <https://doi.org/10.1029/2010JB008156>, 2011.  
915  
916 van Dam, T., Wahr, J. and Lavallée, D.: A comparison of annual vertical crustal displacements from GPS  
917 and Gravity Recovery and Climate Experiment (GRACE) over Europe. *Journal of Geophysical Research:*  
918 *Solid Earth*, 112(B3). <https://doi.org/10.1029/2006JB004335>, 2007.  
919  
920 Van Dam, T., Wahr, J., Milly, P.C.D., Shmakin, A.B., Blewitt, G., Lavallée, D. and Larson, K.M.: Crustal  
921 displacements due to continental water loading. *Geophysical Research Letters*, 28(4), pp.651-654.  
922 <https://doi.org/10.1029/2000GL012120>, 2001.  
923  
924 Velicogna, I., Mohajerani, Y., Landerer, F., Mouginit, J., Noel, B., Rignot, E., Sutterley, T., van den  
925 Broeke, M., van Wessem, M. and Wiese, D.: Continuity of ice sheet mass loss in Greenland and  
926 Antarctica from the GRACE and GRACE Follow-On missions. *Geophysical Research Letters*, 47(8),  
927 p.e2020GL087291. <https://doi.org/10.1029/2020GL087291>, 2020.  
928  
929 Wahr, J., Molenaar, M. and Bryan, F.: Time variability of the Earth's gravity field: Hydrological  
930 and oceanic effects and their possible detection using GRACE. *Journal of Geophysical*  
931 *Research: Solid Earth*, 103(B12), pp.30205-30229. <https://doi.org/10.1029/98JB02844>, 1998.  
932  
933 Wang, H., Xiang, L., Jia, L., Jiang, L., Wang, Z., Hu, B. and Gao, P.: Load Love numbers and Green's  
934 functions for elastic Earth models PREM, iasp91, ak135, and modified models with refined crustal  
935 structure from Crust 2.0. *Computers & Geosciences*, 49, pp.190-199.  
936 <https://doi.org/10.1016/j.cageo.2012.06.022>, 2012.  
937  
938 Watkins, M.M., Wiese, D.N., Yuan, D.N., Boening, C. and Landerer, F.W.: Improved methods for  
939 observing Earth's time variable mass distribution with GRACE using spherical cap mascons. *Journal of*  
940 *Geophysical Research: Solid Earth*, 120(4), pp.2648-2671. <https://doi.org/10.1002/2014JB011547>, 2015.  
941  
942 Wdowinski, S., Bock, Y., Zhang, J., Fang, P. and Genrich, J.: Southern California permanent GPS  
943 geodetic array: Spatial filtering of daily positions for estimating coseismic and postseismic displacements  
944 induced by the 1992 Landers earthquake. *Journal of Geophysical Research: Solid Earth*, 102(B8),  
945 pp.18057-18070. <https://doi.org/10.1029/97JB01378>, 1997.  
946

Deleted: time series

948 Wessel, P., Luis, J.F., Uieda, L., Scharroo, R., Wobbe, F., Smith, W.H. and Tian, D.: The generic  
949 mapping tools version 6. *Geochemistry, Geophysics, Geosystems*, 20(11), pp.5556-5564.  
950 <https://doi.org/10.1029/2019GC008515>, 2019.  
951  
952 Wiese, D.N., Bienstock, B., Blackwood, C., Chrone, J., Loomis, B.D., Sauber, J., Rodell, M., Baize, R.,  
953 Bearden, D., Case, K. and Horner, S.: The mass change designated observable study: overview and  
954 results. *Earth and Space Science*, 9(8), p.e2022EA002311. <https://doi.org/10.1029/2022EA002311>, 2022.  
955  
956 Wiese, D.N., Landerer, F.W. and Watkins, M.M.: Quantifying and reducing leakage errors in the JPL  
957 RL05M GRACE mascon solution. *Water Resources Research*, 52(9), pp.7490-7502.  
958 <https://doi.org/10.1002/2016WR019344>, 2016.  
959  
960 Williams, S.D.: CATS: GPS coordinate [timeseries](#) analysis software. *GPS solutions*, 12(2), pp.147-153.  
961 <https://doi.org/10.1007/s10291-007-0086-4>, 2008.  
962  
963 Williams, S.D., Bock, Y., Fang, P., Jamason, P., Nikolaidis, R.M., Prawirodirdjo, L., Miller, M. and  
964 Johnson, D.J.: Error analysis of continuous GPS position [timeseries](#). *Journal of Geophysical Research: Solid Earth*, 109(B3). <https://doi.org/10.1029/2003JB002741>, 2004.  
965  
966  
967 Wu, S., Nie, G., Liu, J., Wang, K., Xue, C., Wang, J., Li, H., Peng, F. and Ren, X.: A sub-regional  
968 extraction method of common mode components from IGS and CMONOC stations in China. *Remote  
969 Sensing*, 11(11), p.1389. <https://doi.org/10.3390/rs11111389>, 2019.  
970  
971 Yin, G., Forman, B.A., Loomis, B.D. and Luthcke, S.B.: Comparison of Vertical Surface Deformation  
972 Estimates Derived From Space-Based Gravimetry, Ground-Based GPS, and Model-Based Hydrologic  
973 Loading Over Snow-Dominated Watersheds in the United States. *Journal of Geophysical Research: Solid  
974 Earth*, 125(8), p.e2020JB01943. <https://doi.org/10.1029/2020JB019432>, 2020.

Deleted: time series

Deleted: time series